Marco Faenzi, Natalia Graziuso, Enrica Martini, and Stefano Maci

Three simple approaches.

Design Methods for Dual Polarized Metasurface Antennas

Metasurface (MTS) antennas are based on the transformation of a cylindrical-wavefront surface wave (SW) into a general wavefront leaky wave (LW). The MTS aperture is constituted by a grounded dielectric slab printed with an electrically dense distribution of subwavelength patches realizing space-variable, homogenized tensor impedance boundary conditions (IBCs). One of the challenges in this type of antenna is related to obtaining dual polarization operations by using the same impedance modulation. In this article, we explore and compare three simple approaches to obtain two beams with orthogonal polarizations by feeding two ports. A first known method is based on exciting both a transverse electric (TE) and a transverse magnetic (TM) SW mode on the same modulated impedance. A second method exploits the concept of impedance modulation sharing, according to which two distinct modulations, designed to radiate different polarizations when properly illuminated by distinct offset feeding points, are superimposed on the same aperture. A third method consists in duplexing an outward (radially diverging) and an inward (converging to the center) SW. Simple analytical formulas are presented for the synthesis of the impedance that allows for the control of the inward/outward waves to ensure balanced radiation performances in terms of aperture efficiency for the two polarizations. A comparison in terms of performances between the latter two approaches is presented.

INTRODUCTION

Flat, customizable, low-profile antennas with simple, cheap, or limited production costs are assuming a growing importance in the context of modern communication systems like, for instance, satellite links and wireless 5G networks. Currently, such networks are aimed at offering to the end users integrated and fast advanced information access and sharing for real-time and on-demand services. In the near future, it is foreseen that the further development of these network-based advanced services will exploit the potentialities of emerging low-cost antenna technologies. In this rapidly evolving scenario, MTSs [1]–[3] constitute a key technology for realizing smart, conformable, low-cost, and efficient antennas for next-generation communication networks.

A particular class of MTSs consists of those backed by a ground plane; in the microwave regime, they are generally composed of a thin grounded dielectric layer printed on top with a dense texture of subwavelength metallic elements. The macroscopic electrical properties of this artificial surface, which are

Digital Object Identifier 10.1109/MAP.2022.3176782
Date of current version: 24 June 2022

conveniently described in terms of equivalent homogenized boundary conditions, can be accurately controlled by properly designing the local texture geometry in terms of the shape, dimension, and orientation of the constituent subwavelength patches [4]. This type of MTS has been employed to control the wavefront of guided waves [5]–[10] and reflected waves [11]–[14] and the radiation of LWs [15]–[26]. In the latter case, the modulated MTSs behave as radiating apertures by exploiting the local interaction between a TM SW and a locally periodic inductive IBC.

Each SW dominantly interacts with one modulation, while the other (cross) modulation weakly perturbs the incident SW, producing only a minor interference radiation.

The periodic IBC induces Floquet spectral replicas of the exciting SW spectral footprint, with a spectral spacing dictated by the periodicity. Typically, this latter is chosen so that the –1 indexed mode is the only one entering in the visible range, while all other modes are evanescent. This generates an LW mechanism that progressively converts the SW power into space-wave power. A proper design of the local modulation amplitude and phase offers an accurate control of the LW field distribution that allows for tailoring the polarization, amplitude, and phase of the radiating field [30]–[33]. Such ability and flexibility in controlling the radiating aperture field has been exploited recently for designing a number of antennas able to achieve, for instance, high gain [31], [34], high polarization purity [31]–[36], wideband or multifrequency operability [37]–[40], multiple beams [41], [42], and contoured patterns [31], [34], [43], [44]. We note that achieving such challenging features does not alter the overall MTS antenna structure, which remains in all cases simple and extremely low profile—it is only a matter of a proper design of the IBC modulation.

The frequency range of MTS antennas has been recently extended to the subterahertz domain by introducing modulated structures based on metallic pillars [27]–[29], 3D printed on a common ground. Such structures can be fruitfully employed to overcome the hurdles associated to losses due to the use of dielectric substrates at the subterahertz range without losing the capability of an accurate control of the surface mode properties.

Notwithstanding the aforementioned developments, which have sometimes tackled considerably challenging radiation performances, to date only a few works have directly addressed dual polarized aperture design [35], [36]. In [35] and [36], two synchronous TE and TM modes are conveniently excited on the same MTS by a diplexed feed, thus providing orthogonally polarized aperture illuminations. In this article, we examine two different approaches for obtaining dual-polarized broadside radiation from a common aperture. These approaches are characterized by a larger gain bandwidth and a simpler feeding architecture with respect to the one in [35]. Both methods, analogously to [35], are based on the shared use of the same modulated impedance by two orthogonally polarized aperture fields.

In the first of these novel approaches, the sharing of the MTS aperture is based on the concept of *overlapped modulations*: two distinct right-hand/left-hand (RH/LH) homogenized impedance modulations are designed with phase centers located at two separated points and then mathematically superimposed. The resulting interference pattern is next implemented by subwavelength patch elements. Two independent feeding monopoles are located at the two phase centers, so that two outward propagating SWs are launched. Each SW dominantly interacts with one modulation, while the other (cross) modulation weakly perturbs the incident SW, producing only a minor interference radiation.

In the second novel approach, denoted *inward/outward mode aperture sharing*, a centrally launched, outward-directed SW provides a broadside RH circularly polarized (RHCP) pencil beam after interacting with an anisotropic modulated IBC. An inward-propagating SW, centrally converging from the rim of the aperture, is also generated by adding a thin parallel-plate waveguide below the MTS ground, terminated by a circular peripheral corner reflector to provide a 180° E-bend. The inward SW experiences an azimuthal IBC phase progression that is specular with respect to the one seen from the outward mode, thus enabling an LH circularly polarized (LHCP) radiation. The key point, addressed here is the definition of an analytical impedance modulating function for the simultaneous control of outward/inward excitation with similar radiation pattern properties.

The effectiveness of the different approaches for achieving dual polarization is demonstrated by full-wave simulations that also involve the complete design of the metallic texture through elliptical elements.

THE HOMOGENIZED BC MODEL

The antennas we consider possess a circular shape of radius a, and they consist of a homogeneous grounded dielectric slab of thickness h and relative permittivity ε_r printed with a very thin metal texture coating. A cylindrical reference system is introduced, with the z-axis orthogonal to the aperture and its origin at the aperture center. The metallic coating is constituted by densely arranged metallic patches of variable shape and dimensions, and it is modeled through a continuous gently varying anisotropic tensor impedance $j\underline{\underline{\mathbf{X}}}$ characterized by a capacitive average (see Figure 1) [45]. This tensor links the tangential electric field to continuous electric current flowing into the homogenized cladding by [30]

$$\mathbf{E}_t = j\underline{\underline{\mathbf{X}}} \cdot \mathbf{J}, \tag{1}$$

where $\mathbf{E}_t$ represents the tangential component of the electric field at the MTS, and the current $\mathbf{J}$ is related to the discontinuity of the tangential magnetic field across the metallic cladding as $\mathbf{J} = \hat{\mathbf{z}} \times [\mathbf{H}_t|_{z=0^+} - \mathbf{H}_t|_{z=0^-}]$. In the absence of losses, the reactance tensor $\underline{\underline{\mathbf{X}}}$ is Hermitian; if, additionally, the MTS consists of unit cells with two orthogonal symmetry axes, $\underline{\underline{\mathbf{X}}}$ is real and symmetric. In the following, we assume this latter case. For constant-average reactance surfaces supporting a radial SW propagation, the components of the tensor $\underline{\underline{\mathbf{X}}}$ can be conveniently expressed in cylindrical coordinates as

$$\begin{aligned}
\underline{\underline{\mathbf{X}}}(\rho) &= \hat{\rho}\hat{\rho}X_{\rho\rho} + (\hat{\rho}\hat{\phi} + \hat{\phi}\hat{\rho})X_{\rho\phi} + \hat{\phi}\hat{\phi}X_{\phi\phi} \\
X_{\rho\rho}(\boldsymbol{\rho}) &= \bar{X}_{\rho\rho}[1 + m_\rho(\boldsymbol{\rho})\cos(Ks(\boldsymbol{\rho})\boldsymbol{\rho} + \Phi_\rho(\boldsymbol{\rho}))] \\
X_{\rho\phi}(\boldsymbol{\rho}) &= \bar{X}_{\rho\phi}m_\phi(\boldsymbol{\rho})\cos(Ks(\boldsymbol{\rho}) + \Phi_\phi(\boldsymbol{\rho})) \\
X_{\phi\phi}(\boldsymbol{\rho}) &= \bar{X}_{\phi\phi}[1 - m_\rho(\boldsymbol{\rho})\cos(Ks(\boldsymbol{\rho}) + \Phi_\rho(\boldsymbol{\rho}))],
\end{aligned} \tag{2}$$

where $\boldsymbol{\rho}$ is the position vector over the surface. The tensor entry functions in (2) are of the sinusoidal kind, which are characterized by a modulation index $m_\chi(\rho)$ (with $\chi = \rho, \phi$) and by a fast-varying phase $Ks(\boldsymbol{\rho})$ and a slow-varying phase $\Phi_\chi(\boldsymbol{\rho})$. These three parameters control mainly the amplitude, phase, and polarization of the generalized leaky mode on the aperture. An exhaustive explanation of this property is given in [31].

The tensor reactance in (2) is modulated in a sinusoidally oscillating way so as to have a constant, diagonal average, denoted by $\bar{\underline{\underline{\mathbf{X}}}} = \hat{\rho}\hat{\rho}\bar{X}_\rho + \hat{\phi}\hat{\phi}\bar{X}_\phi = \frac{1}{A}\iint_A \underline{\underline{\mathbf{X}}}(\rho)dA$, where A is the circular area of the aperture. This property ensures that the average of the current $\mathbf{J}$ excited in the metallic coating by a vertical monopole can be treated as a perturbation of the current associated with the TM-polarized SW that would be excited by the same source on a nonmodulated MTS, i.e., characterized by a homogenized reactance $\bar{\underline{\underline{\mathbf{X}}}}$. It is noted, however, that, in particular MTS designs, a TE polarized wave also can be excited and supported by the surface (see the next section). For the nonmodulated reactance with TM excitation, the SW current can be expressed as

$$\mathbf{J}_0 = J_0 H_1^{(2)}(\beta_{sw}\rho)\hat{\rho}, \tag{3}$$

where $H_1^{(2)}$ is a Hankel function of the second kind and first order, and β_{sw} is the wavenumber of the unperturbed SW mode. The latter is determined by solving the dispersion equation relevant to the "penetrable" capacitive reactance $\bar{\underline{\underline{\mathbf{X}}}}$ [45] and can also be expressed as $\beta_{sw} = k\sqrt{1 + \bar{X}_0^2/\zeta^2}$, where k and ζ are the free space wavenumber and impedance, respectively, and the term $\bar{X}_0$ is the TM "impenetrable" inductive reactance. This quantity accounts for the contributions of both the metallic cladding and the grounded slab, and it is equal to the ratio of the total tangential electric and magnetic fields at the top interface. For practical MTSs, the wavenumber β_{sw} can be evaluated by a full-wave analysis, as shown in [47] and [48]; a closed-form approximation is available in [45].

The impedance modulation leads to an SW-to-LW conversion [49], gradually damping the SW power due to the LW radiation. This radiation mechanism is modeled by an adiabatic Floquet expansion [30] based on the solution of the local canonical problem [46] that matches the impedance modulation. The average current, representing the dominant 0-indexed mode supported by the modulated reactance, can be derived from (3) by applying a local transformation of the unperturbed wavenumber β_{sw} into a complex wavenumber $\beta_{sw} + \beta_\Delta(\boldsymbol{\rho}) - j\alpha(\boldsymbol{\rho})$. The wave attenuation parameter $\alpha(\boldsymbol{\rho})$ accounts for the radial power leakage associated with the progressive radiation of the SW. The term $\beta_\Delta(\boldsymbol{\rho})$ accounts for the small deviation of the propagation constant from the value associated with the average impedance [30]. Notice that both $\beta_\Delta(\boldsymbol{\rho})$ and $\alpha(\boldsymbol{\rho})$ depend directly on the *local* modulation of the tensor $\underline{\underline{\mathbf{X}}}$. The *global* complex phase of the dominant mode can then be obtained by integrating the ρ-dependent complex wavenumber $\beta_{sw} + \beta_\Delta(\boldsymbol{\rho}) - j\alpha(\boldsymbol{\rho})$ along the SW propagation path. The –1 indexed mode of the adiabatic Floquet expansion of the currents flowing in the coating can thus be approximated as

$$\mathbf{J}^{(-1)} = \mathbf{J}_0^{(-1)} e^{jKs(\rho)} H_1^{(2)}\left(\int_0^\rho [\beta_{sw} + \beta_\Delta(\rho) - \mathrm{j}\alpha(\rho)]d\rho\right), \tag{4}$$

where $\mathbf{J}_0^{(-1)}$ does not depend on the space and $Ks(\rho)$ is the fast-varying part of the impedance tensor in (2). $\mathbf{J}^{(-1)}$ constitutes the "visible" contribution of the total current $\mathbf{J}$ in the far zone of the antenna, that is, $FT_{\mathbf{k}}[\mathbf{J}] \approx FT_{\mathbf{k}}[\mathbf{J}^{(-1)}]$ for $|\mathbf{k}| < k$, where FT indicates the Fourier spectrum operator and $\mathbf{k}$ is the wave vector. We note that the spatial amplitude distribution of the current in (4) depends essentially on the attenuation constant $\alpha(\boldsymbol{\rho})$, while the phase distribution mainly depends on the average value of the impedance and the modulation period. Finally, the polarization properties of the –1 indexed currents can be controlled through a proper design of the phase of the cross-diagonal components of $\underline{\underline{\mathbf{X}}}$ [30] in the case of a TM-polarized exciting

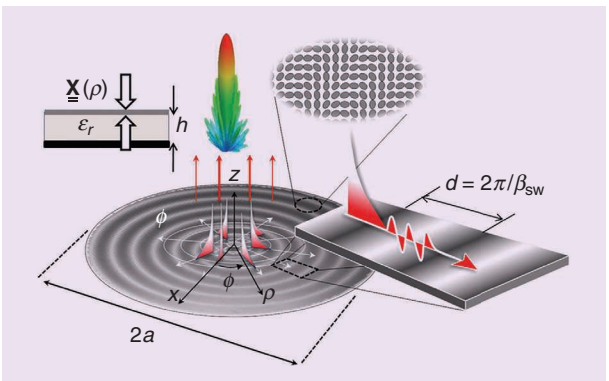

FIGURE 1. The geometry of a modulated MTS aperture. A small monopole is placed at the center of the structure as an SW launcher, and radiation arises from the interference between the cylindrical wavefront SW and the spatially variable BC. The top insets show a sketch of the MTS stack-up and the detail of the subwavelength elements for BC implementation. The bottom inset shows a pictorial representation of the canonical problem that models the SW interaction with the modulated BC.

SW. On the other hand, in the case of TE/TM excitation, the tensor impedance can be taken as diagonal, and polarization is controlled through a proper combination of the exciting modes, as shown next.

DUAL-MODE APERTURE SHARING

A modulated MTS broadside antenna capable of handling dual polarization was designed in [35] and experimentally validated in [36]. Here, we summarize the design approach for the sake of completeness. The MTS is designed so as to simultaneously support two synchronous, decoupled TM_z and TE_z SW modes. The tensor $\underline{\underline{\mathbf{X}}}$ assumes a diagonal shape in the cylindrical reference system; i.e., $\bar{X}_{\phi\rho} = \bar{X}_{\rho\phi} = 0$, and

$$X_{\rho\rho}(\rho) = \bar{X}_{\rho\rho}\left[1 + m_{\mathrm{TM}}\cos\left(\frac{2\pi\rho}{d_{\mathrm{TM}}}\right)\right]$$
$$X_{\phi\phi}(\rho) = \bar{X}_{\phi\phi}\left[1 + m_{\mathrm{TE}}\cos\left(\frac{2\pi\rho}{d_{\mathrm{TE}}}\right)\right]. \quad (5)$$

In (5), $\bar{X}_{\rho\rho}$ and $\bar{X}_{\phi\phi}$ are the average sheet reactances of the TM–TM and TE–TE tensor components, respectively,

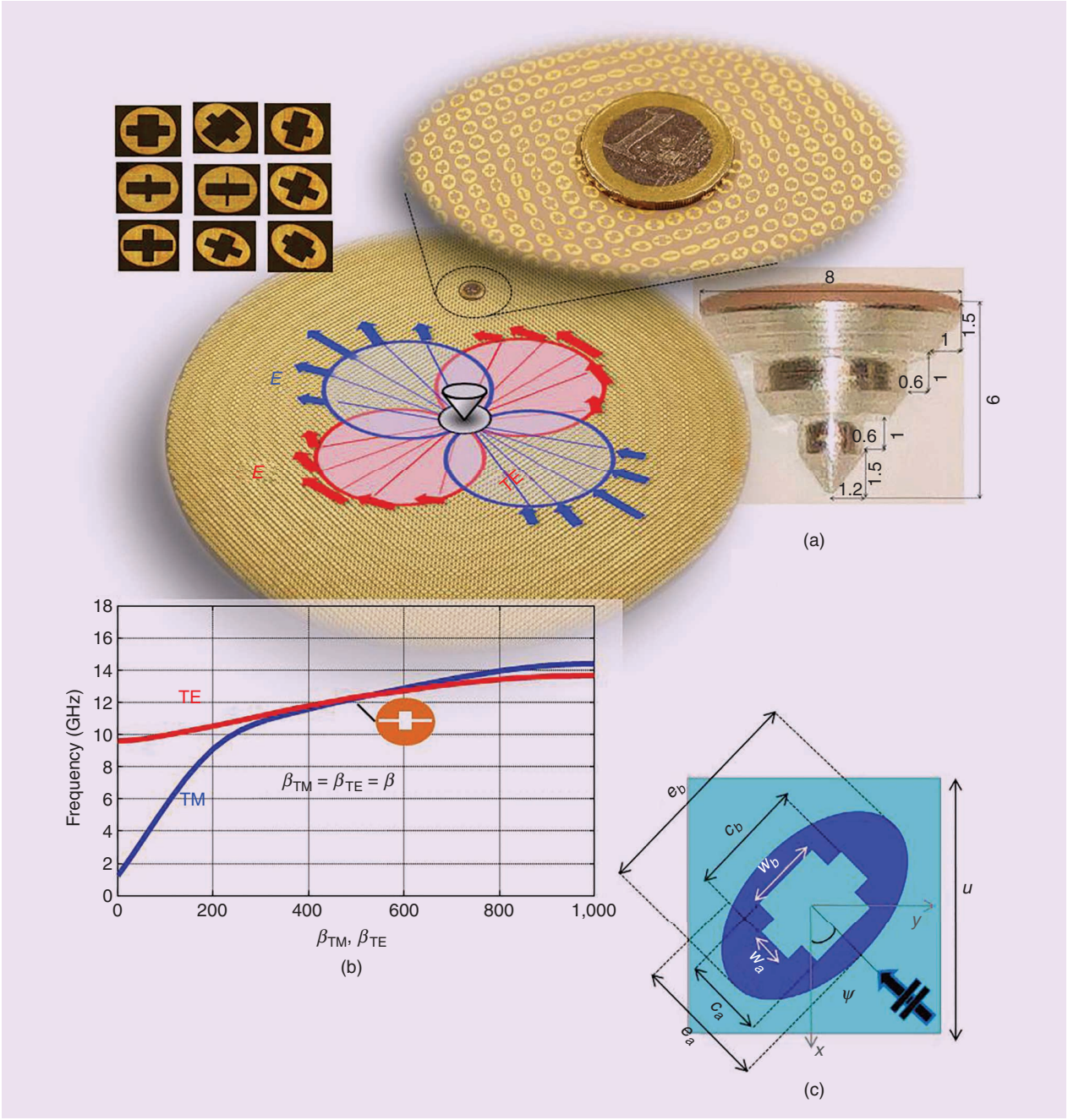

FIGURE 2. The X-band, dual-polarized MTS antenna excited by two modes presented in [35]. (a) A layout of the printed surface with zooms of the elements. The SW pattern for TE and TM modes launched by a circular OEW fed by a single mode is depicted. The OEW is surmounted by a conical metallic hat shown in an inset. (b) The dispersion diagram of the degenerating TE and TM modes. (c) The geometry of the individual elements and design parameters.

which assume negative (capacitive) values. The corresponding impenetrable average reactances $\bar{X}_{0,\rho}$ and $\bar{X}_{0,\phi}$ that are seen from the top of the MTS accounting for the presence of the grounded slab are inductive and capacitive, respectively; namely, they satisfy the condition $\bar{X}_{0,\rho}\bar{X}_{0,\phi} < 0$ for enabling the simultaneous support of a TM and a TE SW mode.

The two independent modulation functions of the tensor reactance able to provide broadside beams with two orthogonal polarizations are superimposed pointwise on the aperture.

The tensor in (5) is implemented through suitable kinds of metal elements that possess geometrical features that allow for a reasonably independent control of the two components in (5). The metal elements chosen in [35] to fulfill such conditions are elliptical patches with a cross-shaped slot (see the top left inset of Figure 2). The cross arms' lengths are varied to control the two diagonal tensor entries.

The feed launches the two degenerating TE and TM modes together on the surface so that they interact in an almost decoupled way with its relevant diagonal entry of the tensor impedance. The excitation of the dual SW mode is provided by an ad hoc feed that is able to independently excite the two modes with the same amplitude for each linear polarization. This is obtained by using a circular open-ended waveguide (OEW) excited by a couple of orthogonal TE11 modes in phase quadrature covered by a conical hat (Figure 1 of [35]); the latter is used to increase the SW launching efficiency. An orthomode transducer (OMT) has been realized to transform the TE10 in two rectangular waveguide ports for the two counterrotating excitations. Figure 2(a) shows the combination of the two surface wave modes when excited by a linearly polarized component only. The design of the modulated MTS is simplified if the TM_z and TE_z modes supported by the average reactance possess the same dispersion characteristics. This property is ensured by the following relationship:

$$\beta_{TM} = \beta_{TE} \Rightarrow k\sqrt{1+\left(\frac{\bar{X}_{0,\rho}}{\zeta}\right)^2} = k\sqrt{1+\left(\frac{\bar{X}_{0,\phi}}{\zeta}\right)^2} \qquad (6)$$

(see the diagram in Figure 2). Equation (6) implies a matching between the dispersion curves of the two modes supported by the same anisotropic impedance, and it corresponds to the balanced (Babinet) condition $\bar{X}_{0,\rho}\bar{X}_{0,\phi} = -\zeta^2$. Under this condition, two independent orthogonally polarized broadside beams are obtained by designing approximately the same modulation periodicities, i.e., by letting $d_{TM} = 2\pi/\beta_{TM}$ and $d_{TE} = 2\pi/\beta_{TE}$ in (6). The radiation patterns obtained for this design are shown in Figure 3. The implementation realized in [35] provided an aperture efficiency of about 33% for both polarizations. The obtained polarization purity has been found to be very good, an outcome that, however, substantially depends on the practical realization of the feeding structure [36].

Concerning the design of the surface that respects (6), one can play with the parameters described in Figure 2(c). It has been discussed in [35] that the choices of the parameters (e_b/u) and (c_b/e_b) mostly affect the TM_z mode (the radial entry of the tensor). However, the parameters (c_a/e_a) and (w_b/u) mostly affect the dispersion of the TE mode (the azimuthal entry of the tensor). It is worth noting that the frequency dispersion is more significant for the TE mode since its working point is closer to the resonance. This implies a difficulty in maintaining a large bandwidth. Furthermore, higher values of the parameters couple (c_b/e_b) are associated with higher TM reactance levels. An analogous trend can be observed when the pixel element becomes larger with respect to a given unit cell side (that is, for larger ratios e_b/u). Instead, the TE reactance can be controlled by

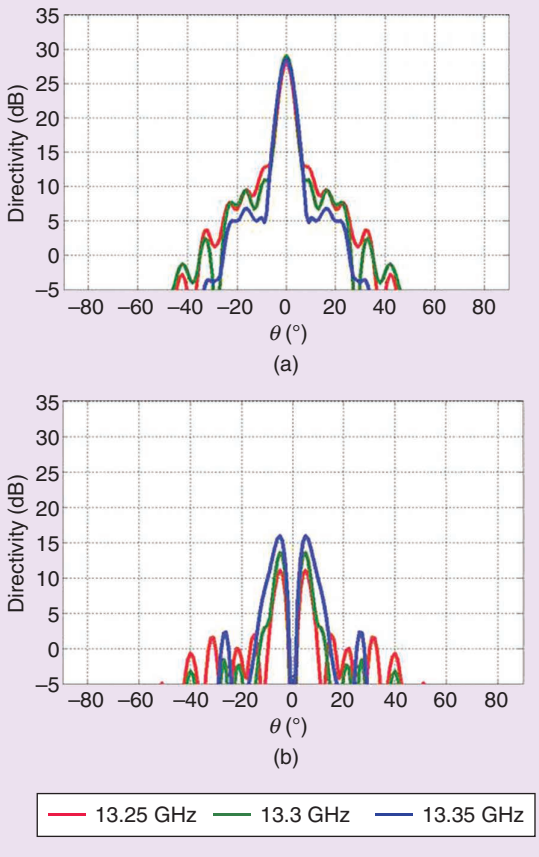

FIGURE 3. The measured dual-polarization MTS antenna directivity patterns for three frequencies in the X-band: (a) LHCP and (b) RHCP (from [36]) when excited at one port only of the OMT.

operating on (e_a/e_b), (c_a/e_a), and (w_b/u); higher values of these latter parameters increase the TE reactance considerably. For the case $\varphi = \psi = 0°$, the curves associated with TM and TE SW dispersion cross at the working frequency ($\beta_{TM} = \beta_{TE}$ at 13.5 GHz), leading to the two modes phase matching in Figure 2(b).

The measured percent –2-dB bilateral relative bandwidth is about 1.8%, which is insufficient for some applications; this is the main drawback of the method.

APERTURE SHARING BY OVERLAPPED MODULATIONS

A dual polarization design can be alternatively obtained by superposition on the same aperture of two distinct modulations with counterrotating (RH and LH) spirals and proper anisotropy, whose phase centers are offset positioned [see Figure 4(a)]. This approach has been used in [41] to implement multiple beams at the same frequency or similar beams at two different frequencies [39], and it is adapted here to obtain dual polarization. The two independent modulation functions of the tensor reactance able to provide broadside beams with two orthogonal polarizations are superimposed pointwise on the aperture [Figure 4(a)]. Two distinct TM monopole feeds are defined and implemented for the two modulations [Figure 4(b)]. Each one can be simply constituted by the inner conductor of a coaxial cable. This makes a significant difference with respect to the method presented in the previous section, where the antenna is excited by a hybrid TE–TM SW launcher.

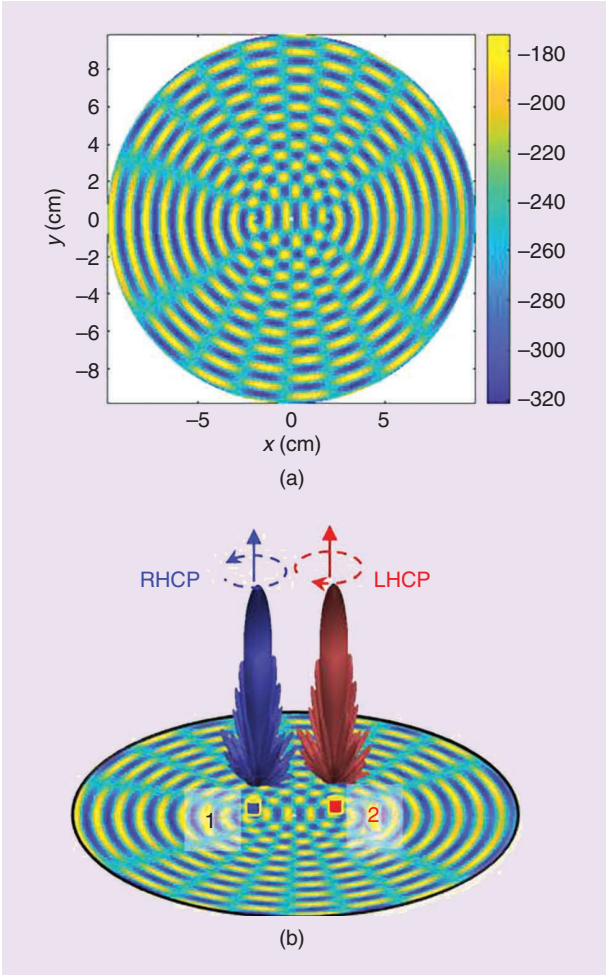

FIGURE 4. Radial component $X_{\rho\rho} = \hat{\rho} \cdot \underline{\underline{\mathbf{X}}} \cdot \hat{\rho}$ of the transparent tensor impedance for (a) overlapped aperture modulations realizing two counterpolarized beams when (b) excited from different feed points. The antenna has a radius of 10 cm, an 8.7 wavelength at an operating frequency of 26.4 GHz, and it is obtained on a substrate with relative permittivity $\varepsilon_r = 6.15$ and thickness $h = 0.635$ mm. The two feed points are located at $\ell = 1.7$ cm from the global reference system center.

To express the global MTS reactance, it is convenient to define two local reference systems, whose origins are located at the feed positions, denoted by $(-1)^n \ell \hat{x}$ $(n = 1, 2)$, where ℓ is the feed distance from the origin of a third, global reference system. The local reference systems possess radial and azimuthal coordinates r_n and ϕ_n, respectively, and relevant radial and azimuthal unit vectors $\hat{\mathbf{r}}_n = \mathbf{r}_n/r_n$ and $\hat{\boldsymbol{\phi}}_n = \hat{\mathbf{z}} \times \hat{\mathbf{r}}_n$ respectively, with $\mathbf{r}_n = \boldsymbol{\rho} - (-1)^n \ell \hat{x}$, and $r_n = |\mathbf{r}_n|$. The global reactance tensor $\underline{\underline{\mathbf{X}}}$ is hence obtained as [41]

$$\underline{\underline{\mathbf{X}}} = \frac{1}{2} U_A \sum_{n=1}^{2} \left(\hat{\rho}_n \hat{\rho}_n X_{rr}^{(n)} + (\hat{\rho}_n \hat{\boldsymbol{\phi}}_n + \hat{\boldsymbol{\phi}}_n \hat{\rho}_n) X_{r\phi}^{(n)} + \hat{\boldsymbol{\phi}}_n \hat{\boldsymbol{\phi}}_n X_{\phi\phi}^{(n)} \right), \tag{7}$$

where $U_A = u(a - \rho)$ is a radial step function that is unity for $\boldsymbol{\rho} \leq a$ and zero for $\boldsymbol{\rho} > a$. In (7), the entries of the transparent reactance tensor $\underline{\underline{\mathrm{X}}}$ are given by

$$\begin{aligned} X_{rr}^{(n)} &= \bar{X}[1 + 2m \cos(\beta_{sw} r_n + (-1)^n \phi_n)] \\ X_{r\phi}^{(n)} &= (-1)^{n-1} \bar{X} 2m \sin(\beta_{sw} r_n + (-1)^n \phi_n) \\ X_{\phi\phi}^{(n)} &= \bar{X}[1 - 2m \sin(\beta_{sw} r_n + (-1)^n \phi_n)]. \end{aligned} \tag{8}$$

The tensor $\underline{\underline{\mathbf{X}}}$ is finally expressed in the global coordinate system by projection over the global unit vectors. In their individual reference system, the two holographies represent two counterrotating spirals.

Exciting the two ports individually provides two counterpolarized beams (RHCP and LHCP). Indeed, when feed 1 is excited, the SW launched on the surface couples coherently with the modulation of spiral modulation 1, and it radiates an RHCP field. On the other hand, the coupling of the SW excited by feed 1 with the modulation of spiral 2 produces a spurious radiation, mainly cross polarized. The mechanism is completely different from the one analyzed in the previous section, where an inherently RHCP (LHCP) incident SW is obtained by playing with a hybrid TE–TM launcher, and thus the cross-diagonal entries of the reactance are zero in the cylindrical reference system. The situation changes in the example examined in this section, where the feeding point is simply constituted by a TM vertical electric dipole launcher, and the cross-diagonal entries of the tensor in each individual reference system are different from zero, to realize the counterrotating spiral holographies.

An example of an aperture-sharing design is illustrated in Figure 4. The antenna has radius $a = 10$ cm, and it is designed to operate at central frequency $f_0 = 26.4$ GHz. The IBC expressed by (8) is implemented on a Rogers RO3006 laminate, which possesses relative permittivity $\varepsilon_r = 6.15$ and thickness $h = 0.635$ mm. The two counter-rotating spiral-type modulations are characterized by a constant modulation index $m = 0.3$ and an average transparent capacitive reactance $\bar{X} = -249\,\Omega$. Figure 4(a) represents the radial component $X_{\rho\rho} = \hat{\rho} \cdot \underline{\underline{\mathbf{X}}} \cdot \hat{\rho}$ of the tensor in the global reference system. The feeds, placed at the center of their respective impedance modulation layouts, are located at a distance $\ell = 1.7$ cm from the center of the global reference system. The directivity of the two feeds

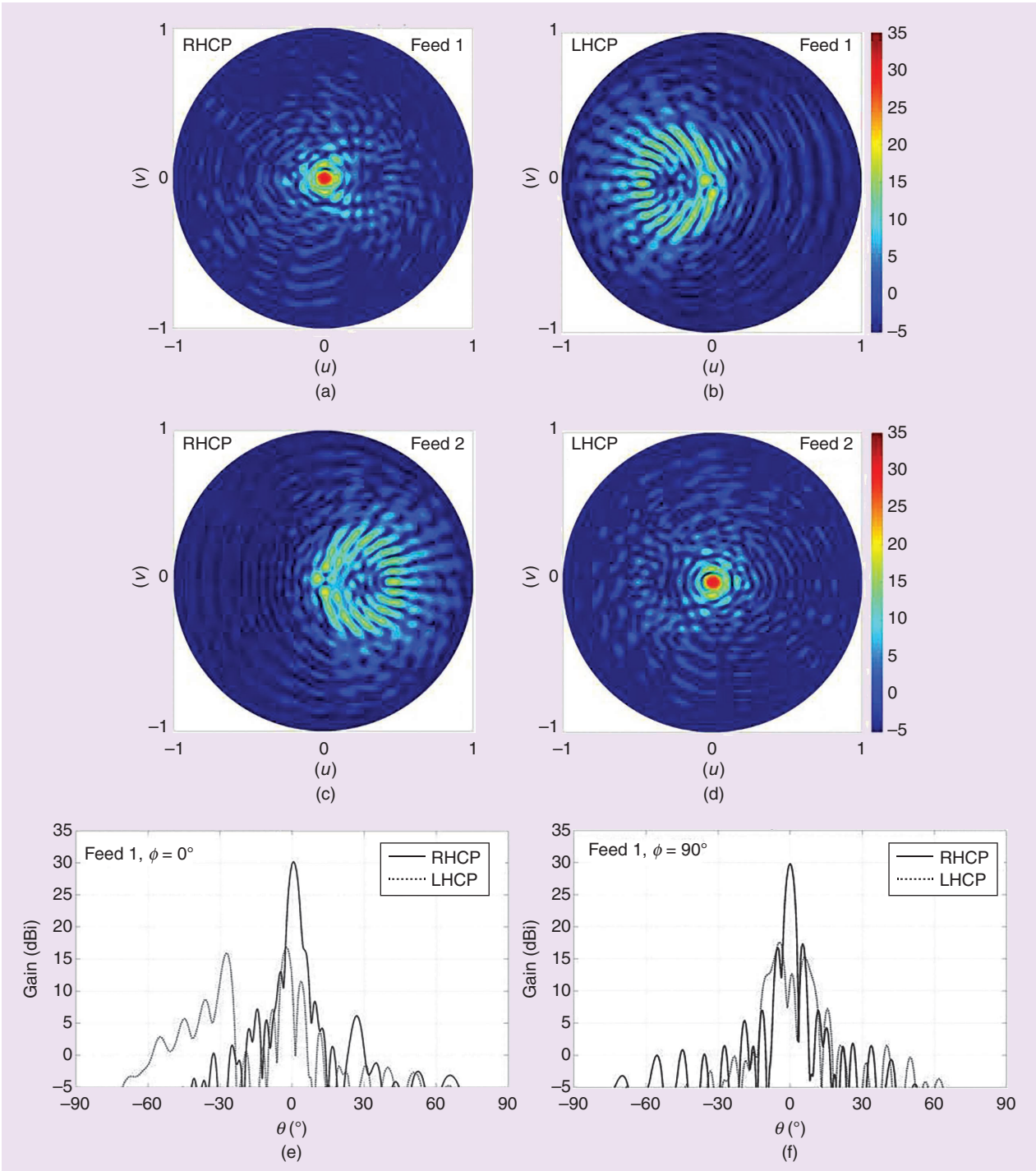

FIGURE 5. (a)–(d) Directivity patterns in the *uv*-plane for the antenna in Figure 4: excitation of (a) and (b) feed 1 and (c) and (d) feed 2. (e) and (f) Directivity patterns in the two orthogonal planes: (e) feed 1, $\phi = 0^\circ$ and (f) feed 2, $\phi = 90^\circ$. Numerical results have been obtained with the homogeneous impedance MOM described in [51]. MOM: method of moments.

is about 30 dB, with an aperture efficiency of about 33% for each case.

The radiation patterns shown in Figure 5(a)–(d) (directivity patterns in the uv-plane) and Figure 5(e) and (f) (principal cuts along $\phi = 0°, 90°$) have been obtained with a full-wave analysis based on homogenized impedance [51]. An aperture efficiency of about 30% has been obtained for both polarizations. We observe that the cross-polarization performance for feed 1 exhibits a zone of increase around a circle in a uv-plane [see Figure 5(b)] because of the interference of SW 1 with modulation 2. The symmetric situation occurs for feed 2 [Figure 5(c)].

It is also worth remarking that a dual polarized aperture based on modulated IBCs excited by two feeds can also be obtained by an inverse problem solution approach based on a direct use of the method of moments (MOM) formulation, as described in [42]–[44].

INWARD/OUTWARD APERTURE SHARING

In this section, we present a novel, alternative design technique for obtaining an aperture able to simultaneously address two broadside beams (RHCP and LHCP) based on radially diverging (outward) and converging (inward) SW propagation. The diverging SW is provided by a centrally located vertical monopole feed, similar to the solutions addressed in previous sections. The inward SW, i.e., the one propagating from the periphery to the center of the aperture, can instead be obtained by a stacked parallel-plate waveguide arrangement in the back of the MTS ground, as pictured in Figure 6(a). A triaxial cable may be adopted for feeding the two ports, and such a realistic feeding system is currently under development. A similar feeding arrangement was proposed in [52] to obtain a dual-polarized radial line slot antenna. In the numerical model presented here, the convergent SW is reproduced by peripheral in-phase vertical monopoles disposed along the outer aperture circumference at relative distance $\lambda_{sw}/2$ (where λ_{sw} is the SW wavelength at the center frequency).

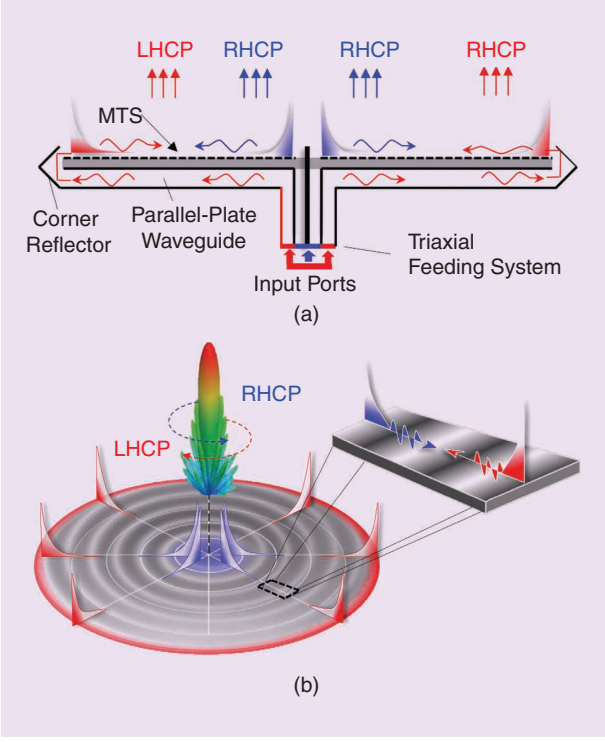

FIGURE 6. A dual polarized MTS antenna obtained with central and peripheral excitations. (a) Triaxial feed mechanism. (b) The outward (blue) and inward (red) SWs excited from the center and from the periphery, respectively. In the zoom: local canonical problem for finding the link between $a(\rho)$ and $m(\rho)$.

Both SWs are supported by the same surface, described by the following IBC tensor entries:

$$\begin{aligned} X_{\rho\rho}(\boldsymbol{\rho}) &= \bar{X}[1 + m(\rho)\cos(\tfrac{2\pi}{d}\rho - \phi)] \\ X_{\rho\phi}(\boldsymbol{\rho}) &= \bar{X}\, m(\rho)\cos(\tfrac{2\pi}{d}\rho - \phi) \\ X_{\phi\phi}(\boldsymbol{\rho}) &= \bar{X}[1 - m(\rho)\cos(\tfrac{2\pi}{d}\rho - \phi)], \end{aligned} \tag{9}$$

where the modulation period d is linked to the value of the SW propagation constant through $\beta_{sw} = 2\pi/d$. The modulation index function $m(\rho)$ affects mainly the behavior of the leakage parameter $\alpha(\rho)$.

We stress that the design of a radially nonuniform leakage parameter $\alpha(\rho)$ allows for the control of the radiating field radial amplitude. The desired attenuation constant profile is obtained by setting a nonuniform modulation index $m(\rho)$. The link between the modulation index and the relevant attenuation constant is given by the solution of the canonical problem that matches the local modulation and the SW cylindrical wavefront with a planar wavefront/1D modulation problem [30] [see the zoom of Figure 6(b)]. In the present design, the proper design of $\alpha(\rho)$ assumes a primary importance for radiation efficiency and polarization purity control. Indeed, the inherent impairment of this configuration is due to the presence of a caustic that the convergent (inward) wave exhibits at the center of the aperture. Consequently, if a nonnegligible amount of inward SW power crosses the caustic, the residual power, if not properly reabsorbed by the feed, generates an outward SW that radiates a cross-polarized field. In any case, such a phenomenon can be handled either by absorbing the inward wave through a matched load terminating the feed or by designing the function $\alpha(\rho)$, as shown next.

It is important to observe that the local solution that establishes the link between $m(\rho)$ and $\alpha(\rho)$ is invariant with respect to the SW propagation direction. Thus, the leakage function $\alpha(\rho)$ is unique for both the inward and the outward SW modes [see the zoom of Figure 6(b)]. However, the same modulation index produces different effects on the (–1)-mode aperture field distribution for the two modes. Indeed, the amplitude profile of the (–1)-mode is determined by combining the SW cylindrical spreading factor and the progressive radial power loss due to the radiation. According to (4), the amplitude of

the (–1) current mode follows an asymptotic behavior of the type $\exp\left(-\int_0^{\rho}\alpha(\rho)d\rho\right)/\sqrt{\rho}$. On the other hand, as the inward wave travels toward the center, i.e., for decreasing radial distances, its asymptotic amplitude envelope is ruled by $\exp(-\int_{\rho}^{a}\alpha(\rho)d\rho)/\sqrt{\rho}$. As expected, the polarization of the currents of the (–1) mode in (4) is indeed orthogonal, because of the change of directon of the SW propagation vector. However, without a proper control of $\alpha(\rho)$, the two cross-polarized-beam gains and beamwidths may be significantly different, which is undesirable in practical applications. Therefore, the objective is to design a nonuniform leakage function $\alpha(\rho)$ that provides a well-balanced pattern beamwidth for the two directions of propagation. To this end, we observe that the overall aperture efficiency depends mainly on the product of two distinct parameters: the spillover efficiency ε_s and the tapering efficiency ε_t [33]. We remark that, to maintain a high polarization purity for the inward excitation, a strict constraint on the spillover efficiency value must be applied at the design stage; this serves to ensure that a negligible amount of inward SW power reaches the central caustic.

Building on the developments presented in [33], it is convenient to consider first the relation between the leakage function $\alpha(\rho)$ and the corresponding radial power distribution functions $S_{o,i}(\rho)$, where the subscripts o and i stand for the outward and inward waves, respectively. It has been shown in [33] that the pair of functions $S_o(\rho)$, $\alpha(\rho)$ are related to each other by the following pair of direct–inverse relationships:

$$\alpha(\rho)=\frac{\frac{\rho S_o(\rho)}{2}}{\frac{1}{\varepsilon_s}p_{\text{rad}}^{(o)}-\int_0^{\rho}S_o(\rho')\rho'd\rho'} \tag{10}$$

$$S_o(\rho)=\frac{2}{\rho}\alpha(\rho)\frac{p_{\text{rad}}^{(o)}}{\varepsilon_s}e^{-2\int_0^{\rho}\alpha(\rho')d\rho'}, \tag{11}$$

where $p_{\text{rad}}^{(o)}$ is the total amount of power radiated by the outward SW along an elemental angular sector; that is, $p_{\text{rad}}^{(o)}=\int_0^a S_o(\rho')\rho'd\rho'$, and ε_s is the spillover efficiency defined as the ratio between the radiated power and the SW power launched by the feed, i.e., $\varepsilon_s=p_{\text{rad}}^{(o)}/p_{\text{SW}}^{(o)}$.

The inverse and direct relationships (10) and (11) are derived in [30] under the nonrestrictive hypothesis of an ideal feed, with unitary feed efficiency in SW excitation. Similar relations can be derived for inward propagation; i.e., in this case, the pair of ρ-dependent functions $S_i(\rho)$, $\alpha(\rho)$ are related to each other by

$$\alpha(\rho)=\frac{\frac{\rho S_i(\rho)}{2}}{\frac{p_{\text{rad}}^{(i)}}{\varepsilon_s}-\int_{\rho}^{a}S_i(\rho')\rho'd\rho'} \tag{12}$$

$$S_i(\rho)=\frac{2}{\rho}\alpha(\rho)\frac{p_{\text{rad}}^{(i)}}{\varepsilon_s}e^{-2\int_{\rho}^{a}\alpha(\rho')d\rho'}, \tag{13}$$

where $p_{\text{rad}}^{(i)}$ represents the power radiated by an elemental sector of unit angle; that is, $p_{\text{rad}}^{(i)}=\int_0^a S_i(\rho')\rho'd\rho'$.

We stress that the leakage constant $\alpha(\rho)$ is invariant with respect to the wave propagation direction. Also, it is not restrictive to assume that the spillover efficiency ε_s is the same inside (11) and (13) and that the radiated power is the same for inward and outward waves $p_{\text{rad}}^{(o)}=p_{\text{rad}}^{(i)}\doteq p_{\text{rad}}$. On the other hand, the two functions $S_{o,i}(\rho)$ have a different form, even when $\alpha(\rho)$ is the same, because of the different integration intervals in (11) and (13). As already mentioned, among the several strategies that one can follow for the design (which depend on the specific antenna requirements), we present here a simple one with the objective to equalize as much as possible the maximum directivity for the inward and the outward traveling modes. To this end, we start by designing $\alpha(\rho)$; then we obtain $S_{o,i}(\rho)$ by using (11) and (13). It is convenient to choose the leakage function $\alpha(\rho)$ of the form

$$\alpha(\rho)=\gamma\frac{f'(\rho)}{1+f(\rho)}, \tag{14}$$

where γ is an arbitrary real positive nondimensional parameter, f is a positive, derivable, monotonically increasing "generating"

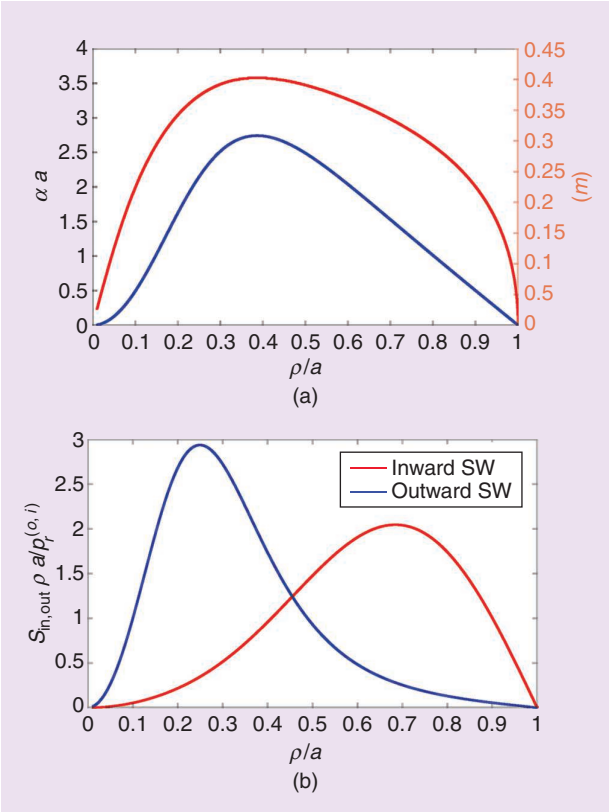

FIGURE 7. (a) Blue curve, LHS vertical scale: normalized leakage parameter $\alpha(\rho)$ in (14) as a function of the normalized distance ρ/a (where a is the antenna radius) optimized for having the same aperture efficiency for the inward and outward cases; red curve, RHS vertical scale: modulation function $m(\rho)$ obtained by the solution of the local 2D problem with average impedance $\bar{X}=-249\ \Omega$ and dielectric substrate with $\varepsilon_r=6.15$ and $h=0.635$ mm. (b) Distribution of the inward and outward power density multiplied by ρa and normalized to the radiated power. LHS: left-hand side.

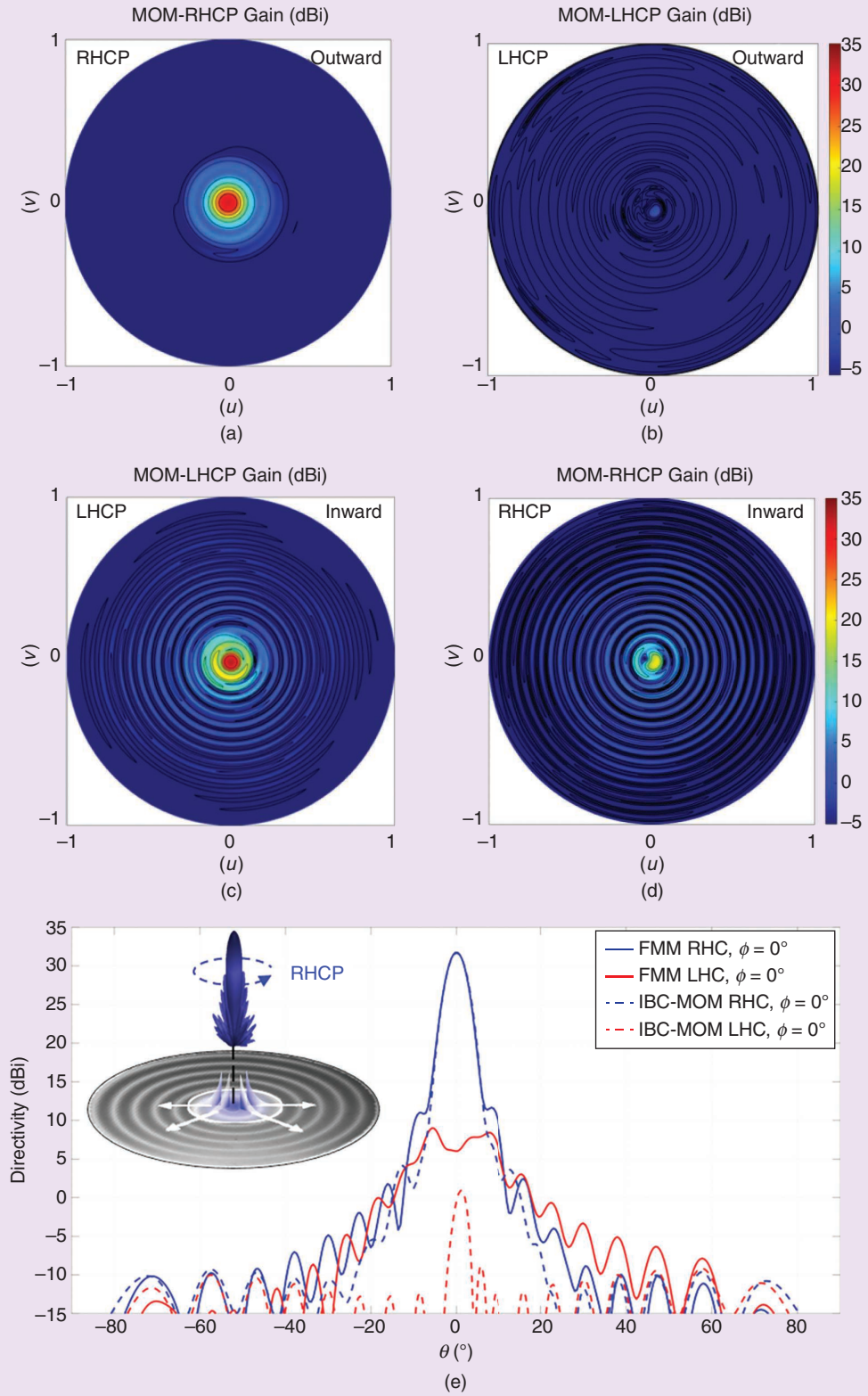

FIGURE 8. (a)–(d) Directivity patterns in the *uv*-plane at an operating frequency of 26.4 GHz for an antenna with radius 10 cm ($a = 8.7\lambda$) printed on a substrate with $\varepsilon_r = 6.15$ and $h = 0.635$ mm. (a) outward wave, RHCP; (b) outward wave, LHCP; (c) inward wave, LHCP; and (d) inward wave, RHCP. (e) and (f) Gain patterns in the plane $\phi = 0$: (e) outward surface wave and (f) inward surface wave. Numerical results obtained from the full-wave analysis of the elliptical-patch based structure are compared with the ones obtained with the homogeneous impedance MOM described in [51]. (*Continued*)

function, and f' denotes its derivative with respect to ρ. The function f may depend on an arbitrary number of parameters (not explicitly written in the notation), and for $\rho = a$ and $\rho = 0$ it must assume the following values:

$$f(a) = \left((1-\varepsilon_s)^{-\frac{1}{2\gamma}} - 1\right) \quad ; \quad f(0) = 0. \tag{15}$$

Since the function f is positive and increases monotonically, a positive value of the leakage function $\alpha(\rho)$ is obtained from (14). Note also that the class of functions used in (14) to represent $\alpha(\rho)$ is such that, when the latter is inserted in both (11) and (13), a closed-form expression is obtained for both $S_{\mathrm{i}}(\rho)$ and $S_{\mathrm{o}}(\rho)$, namely:

$$\frac{S_{\mathrm{o}}(\rho)}{p_{\mathrm{rad}}} = \frac{2}{\rho\varepsilon_s}\frac{\alpha(\rho)}{[1+f(\rho)]^{2\gamma}} \tag{16}$$

$$\frac{S_i(\rho)}{p_{\mathrm{rad}}} = \frac{2}{\rho}\frac{1-\varepsilon_s}{\varepsilon_s}\alpha(\rho)[1+f(\rho)]^{2\gamma}. \tag{17}$$

It can be seen that integrating the right-hand side (RHS) of either (16) or (17) in $\rho\ d\rho$ obtains unity because of (15).

Concerning the tapering efficiency, for the outward wave, one can evaluate the tapering efficiency by using equation (23) in [33]:

$$\varepsilon_{\mathrm{tap}}^{(\mathrm{o})} = \frac{2}{a^2}\frac{\left|\int_0^a \sqrt{\frac{S_{\mathrm{o}}(\rho)}{p_{\mathrm{rad}}}}\,\rho d\rho\right|^2}{\int_0^a \left[\frac{S_{\mathrm{o}}(\rho)}{p_{\mathrm{rad}}}\right]\rho d\rho}. \tag{18}$$

Concerning the inward wave, the expression is quite different since the presence of the central caustic of the (0)-mode, that generates a (0)-mode outward wave with power input for unit azimuthal angle equal to $(1-\varepsilon_s)p_{\mathrm{rad}}$. Therefore, an appropriate approximation of the denominator in the analog of (18) is

$$\varepsilon_{\mathrm{tap}}^{(i)} = \frac{2}{a^2}\frac{\left|\int_0^a \sqrt{\frac{S_i(\rho)}{p_{\mathrm{rad}}}}\,\rho d\rho\right|^2}{\int_0^a \left[\frac{S_i(\rho)}{p_{\mathrm{rad}}} + \frac{(1-\varepsilon_s)S_{\mathrm{o}}(\rho)}{p_{\mathrm{rad}}}\right]\rho d\rho}, \tag{19}$$

where the second term in the denominator accounts for the power radiated by the (–1) mode in the counterpolarized wave due to the mechanism of caustic crossover. Inserting (16) and (17) in (18) and (19) permits a simultaneous control of the tapering aperture efficiency for both the outward and inward cases by optimizing the difference $|\varepsilon_{\mathrm{tap}}^{(i)} - \varepsilon_{\mathrm{tap}}^{(o)}|$ with respect to the generating function f parameters.

As a simple example, we use the parametric generating function $f(\rho) = f(a)\sin^{2n}(\pi\rho/2a)$, where n is a real positive number. We minimize the objective function defined as $|\varepsilon_{t,\mathrm{i}} - \varepsilon_{t,\mathrm{o}}|$ for a fixed value of the spillover efficiency $\varepsilon_s = 0.95$.

This approach leads to $\gamma = 0.8$ and $n = 1.5$. The resulting function $\alpha(\rho)$ (normalized to $1/a$) is represented in Figure 7(a). In the same figure, we have also depicted the corresponding value of $m(\rho)$ obtained by the solution of the local 2D problem with average impedance $\bar{X} = -249\,\Omega$ and dielectric substrate with relative permittivity $\varepsilon_{\mathrm{r}} = 6.15$ and thickness $h = 0.635$ mm (these

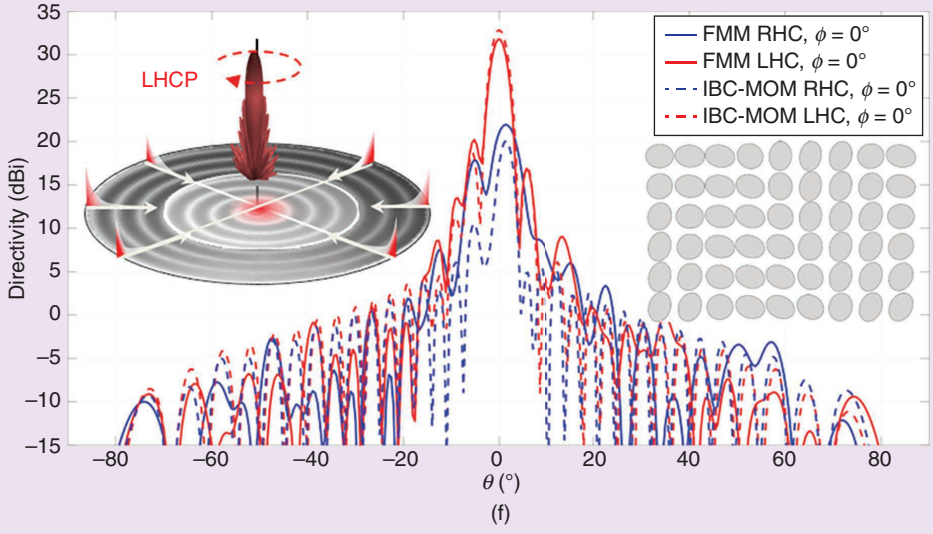

FIGURE 8. (Continued) (a)–(d) Directivity patterns in the *uv*-plane at an operating frequency of 26.4 GHz for an antenna with radius 10 cm ($a = 8.7\lambda$) printed on a substrate with $\varepsilon_{\mathrm{r}} = 6.15$ and $h = 0.635$ mm. (a) outward wave, RHCP; (b) outward wave, LHCP; (c) inward wave, LHCP; and (d) inward wave, RHCP. (e) and (f) Gain patterns in the plane $\phi = 0$: (e) outward surface wave and (f) inward surface wave. Numerical results obtained from the full-wave analysis of the elliptical-patch based structure are compared with the ones obtained with the homogeneous impedance MOM described in [51].

values are the same as those in the case of Figure 4). The distributions of the inward and outward normalized power density are presented in Figure 7(b).

The final antenna has been designed with the same substrate, radius (10 cm), and operating frequency (26.4 GHz) as the one shown in Figure 4 to allow for a better comparison. The antenna directivity patterns in the *uv*-plane are presented in Figure 8(a)–(d). These patterns have been obtained by using the full-wave MOM analysis with homogenized impedance presented in [51]. The homogenized impedance has also been implemented through printed elliptical patches.

The final antenna has been simulated through a fast multipole MOM based on the elliptical domain basis functions described in [8]. The directivity patterns in the two principal planes are compared in Figure 8(e) and (f) with the ones provided by the MOM based on homogenized impedance in [51] with an excellent agreement. We note that the obtained maximum directivity values in the two cases are 31.66 dB for the outward case and 32.84 dB for the inward case, as predicted by the homogenized impedance MOM. Concerning indeed the fast multipole method (FMM) results obtained by the actual printed structure, these are 31.72 dB and 31.77 dB for the inward and outward case respectively,

TABLE 1. COMPARISON BETWEEN MAIN PARAMETERS FROM DIFFERENT DUAL POLARIZED ANTENNAS.

	Design Type	Test	Radius in Wavelengths	Aperture Efficiency (ε_{tot})	Maximum Directivity (Both Polarized) [dBi]	XPD [dB]	2-dB Relative BW [%]	BW × ε_{tot} [%]
Section "Dual-Mode Aperture Sharing"	**Dual mode**	**Full-wave analysis (MOM in [52])**	7.93	0.33	29.09	18	1.8	0.59
		Measurements	7.93	0.21	27.10	17	1.8	0.38
Section "Aperture Sharing by Overlapped Modulations"	**Overlapped modulation**	**Full-wave analysis (MOM in [52])**	8.8	0.33	30.04	16	4	1.32
Section "Inward/Outward Aperture Sharing"	**Inward/outward**	**Full-wave analysis (FMM MOM [34])**	8.8	0.49	31.7	25	4.3	2.1

XPD: cross-polar discrimination; BW: bandwidth.

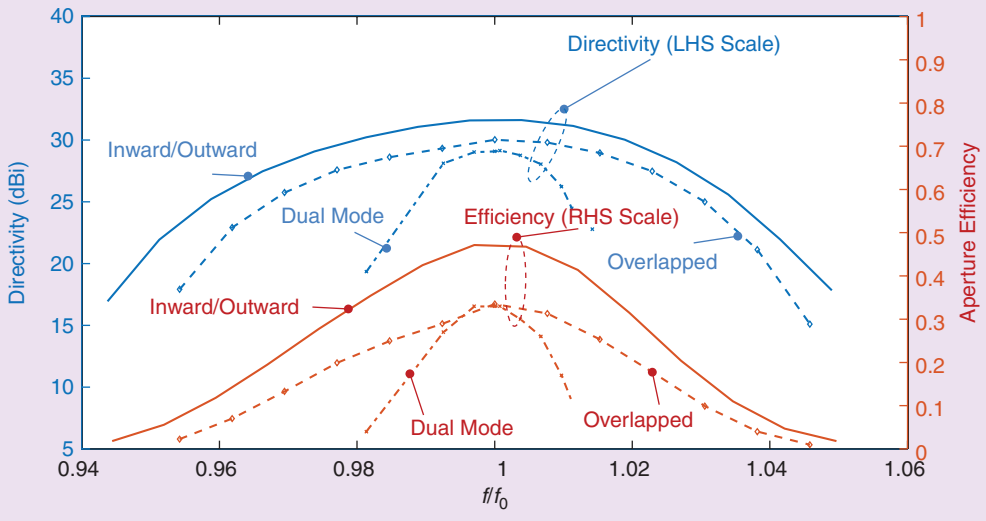

FIGURE 9. Broadside directivity (blue lines, LHS scale) and efficiency (red lines, RHS scale) for the cases studied in this article. (Dual mode, dash-dotted line; overlapped modulations, dashed lines; inward/outward modes, solid lines.)

which corresponds to an overall aperture efficiency of 50%, obtained to have the same gain for the two beams. It is worth noting that, although the goal of equal gain has been reached, the beamwidth of the inward case is narrower with respect to the one of the outward case. The reason for this latter issue is due to the power radiated in the cross-polarized beam, which is much larger in the inward case because of the caustic-point crossover.

CONCLUSIONS

This article has presented three different approaches for the design of dual-polarized MTS antennas. The first one is based on the simultaneous excitation of a TE and a TM SW mode, already documented in a previous couple of publications [35], [36]. Although a quite good level of purity of beam can be obtained, the drawback of this approach is a narrow frequency bandwidth. The second approach exploits overlapped modulations associated to orthogonal circular polarizations and off-centered feeds. The third method achieves dual polarization by exciting both a radially outward traveling TM SW and an inward traveling TM SW. For this latter case, new analytical design formulas have been provided. The inward/outward approach allows for a better aperture efficiency and bandwidth with clean azimuthally symmetric copolarized beam, but with the inward mode affected by a higher cross-polar level in the broadside direction. The approach with overlapped modulation allows for beams that are essentially equal to each other, with a drawback of cross-polarized components far out from the axis. However, this impairment can be reduced by a matched load in the inward port, neglected in our simulations.

The performances of the three approaches proposed are shown in Table 1 and Figure 9. Table 1 summarizes the bilateral fractional bandwidth (defined at –2 dB), efficiency, maximum directivity, and cross-polar discrimination (XPD) for the three cases. In the dual-mode method documented in [36], the dual polarized aperture has a radius of $7.93\lambda_0$ at center frequency, which is thus comparable with the ones tested with the other two methods ($8.8\lambda_0$), even if done at a different central frequency. For the dual-mode case, we have reported in Table 1 the values obtained by both the full-wave analysis and by the measurements [36]. The results of gain and aperture efficiency provided by the three methods are also reported in Figure 9 as a function of the normalized frequency. Other strategies of optimization are under study for the latter two approaches and will be the subject of future works.

ACKNOWLEDGMENTS

We wish to thank Gabriele Minatti and Francesco Caminita of Wave-Up Srl for useful discussions on this subject.

AUTHOR INFORMATION

Marco Faenzi (faenzi@diism.unisi.it) is a researcher in the Department of Information Engineering and Mathematics, University of Siena, 53100, Siena, Italy. His research interests include modulated metasurface apertures and numerical methods for metasurface analysis. He was a recipient of the IEEE Schelkunoff Transaction Prize in 2016.

Natalia Graziuso (natalia.graziuso@student.unisi.it) is with the Department of Information Engineering and Mathematics, University of Siena, 53100, Siena, Italy. She is attaining her MS degree in telecommunications engineering. During her BD thesis, she helped develop dual polarized metasurface antenna designs.

Enrica Martini (martini@diism.unisi.it) is an associate professor in the Department of Information Engineering and Mathematics, University of Siena, 53100, Siena, Italy. Her research interests include metasurface and metamaterial characterization, metasurface-based antennas and microwave devices, electromagnetic scattering, antenna measurements, and tropospheric propagation. She is a Senior Member of IEEE.

Stefano Maci (macis@diism.unisi.it) is a full professor in the Department of Information Engineering and Mathematics, University of Siena, 53100, Siena, Italy. He received the IEEE Schelkunoff Transaction Prize, Chen-To Tai Distinguished Educator Award, and International Union of Radio Science Dellinger Gold Medal. He is a Fellow of IEEE.

REFERENCES

[1] C. L. Holloway, E. F. Kuester, J. A. Gordon, J. O'Hara, J. Booth, and D. R. Smith, "An overview of the theory and applications of metasurfaces: The two-dimensional equivalents of metamaterials," *IEEE Antennas Propag. Mag.*, vol. 54, no. 2, pp. 10–35, Apr. 2012, doi: 10.1109/MAP.2012.6230714.

[2] S. B. Glybovski, S. A. Tretyakov, P. A. Belov, Y. S. Kivshar, and C. R. Simovski, "Metasurfaces: From microwaves to visible," *Phys. Rep.*, vol. 634, pp. 1–72, May 2016, doi: 10.1016/j.physrep.2016.04.004.

[3] A. Christos *et al.*, "Synthesis of electromagnetic metasurfaces: Principles and illustrations," *EPJ Appl. Metamater.*, vol. 2, no. 12, pp. 1–11, 2015, doi: 10.1051/epjam/2015016.

[4] A. M. Patel and A. Grbic, "The effects of spatial dispersion on power flow along a printed-circuit tensor impedance surface," *IEEE Trans. Antennas Propag.*, vol. 62, no. 3, pp. 1464–1469, Mar. 2014, doi: 10.1109/TAP.2013.2294196.

[5] S. Maci, G. Minatti, M. Casaletti, and M. Bosiljevac, "Metasurfing: Addressing waves on impenetrable metasurfaces," *IEEE Antennas Wireless Propag. Lett.*, vol. 10, pp. 1499–1502, Dec. 2011, doi: 10.1109/LAWP.2012.2183631.

[6] A. M. Patel and A. Grbic, "Transformation electromagnetics devices based on printed-circuit tensor impedance surfaces," *IEEE Trans. Microw. Theory Techn.*, vol. 62, no. 5, pp. 1102–1111, May 2014, doi: 10.1109/TMTT.2014.2314440.

[7] A. M. Patel and A. Grbic, "Effective surface impedance of a printed-circuit tensor impedance surface (PCTIS)," *IEEE Trans. Microw. Theory Techn.*, vol. 61, no. 4, pp. 1403–1413, Apr. 2013, doi: 10.1109/TMTT.2013.2252362.

[8] M. Mencagli, E. Martini, and S. Maci, "Surface wave dispersion for anisotropic metasurfaces constituted by elliptical patches," *IEEE Trans. Antennas Propag.*, vol. 63, no. 7, pp. 2992–3003, Jul. 2015, doi: 10.1109/TAP.2015.2422352.

[9] N. Yu and F. Capasso, "Flat optics with designer metasurfaces," *Nature Mater.*, vol. 13, no. 2, pp. 139–150, 2014, doi: 10.1038/nmat3839.

[10] M. Mencagli, C. Della Giovampaola, and S. Maci, "A closed-form representation of isofrequency dispersion curve and group velocity for surface waves supported by anisotropic and spatially dispersive metasurfaces," *IEEE Trans. Antennas Propag.*, vol. 64, no. 6, pp. 2319–2327, Jun. 2016, doi: 10.1109/TAP.2016.2547021.

[11] N. Yu *et al.*, "Light propagation with phase discontinuities: Generalized laws of reflection and refraction," *Science*, vol. 334, no. 6054, pp. 333–337, 2011, doi: 10.1126/science.1210713.

[12] N. Mohammadi Estakhri and A. Alù, "Wave-front transformation with Gradient metasurfaces," *Phys. Rev. X*, vol. 6, no. 4, p. 041008, Oct. 2016, doi: 10.1103/PhysRevX.6.041008.
[13] A. M. H. Wong and G. V. Eleftheriades, "Perfect anomalous reflection with a Bipartite Huygens' metasurface," *Phys. Rev. X*, vol. 8, no. 1, p. 011036, Feb. 2018, doi: 10.1103/PhysRevX.8.011036.
[14] J. Budhu and A. Grbic, "Perfectly reflecting metasurface reflectarrays: Mutual coupling modeling between unique elements through homogenization," *IEEE Trans. Antennas Propag.*, vol. 69, no. 1, pp. 122–134, Jan. 2021, doi: 10.1109/TAP.2020.3001450.
[15] B. H. Fong, J. S. Colburn, J. J. Ottusch, J. L. Visher, and D. F. Sievenpiper, "Scalar and tensor holographic artificial impedance surfaces," *IEEE Trans. Antennas Propag.*, vol. 58, no. 10, pp. 3212–3221, Oct. 2010, doi: 10.1109/TAP.2010.2055812.
[16] G. Minatti, F. Caminita, M. Casaletti, and S. Maci, "Spiral leaky-wave antennas based on modulated surface impedance," *IEEE Trans. Antennas Propag.*, vol. 59, no. 12, pp. 4436–4444, Dec. 2011, doi: 10.1109/TAP.2011.2165691.
[17] A. M. Patel and A. Grbic, "A printed leaky-wave antenna based on a sinusoidally-modulated reactance surface," *IEEE Trans. Antennas Propag.*, vol. 59, no. 6, pp. 2087–2096, Jun. 2011, doi: 10.1109/TAP.2011.2143668.
[18] G. Minatti *et al.*, "Modulated metasurface antennas for space: Synthesis, analysis and realizations," *IEEE Trans. Antennas Propag.*, vol. 63, no. 4, pp. 1288–1300, Apr. 2015, doi: 10.1109/TAP.2014.2377718.
[19] G. Minatti, S. Maci, P. De Vita, A. Freni, and M. Sabbadini, "A circularly-polarized isoflux antenna based on anisotropic metasurface," *IEEE Trans. Antennas Propag.*, vol. 60, no. 11, pp. 4998–5009, Nov. 2012, doi: 10.1109/TAP.2012.2208614.
[20] M. Faenzi *et al.*, "Realization and measurement of broadside beam modulated metasurface antennas," *IEEE Antennas Wireless Propag. Lett.*, vol. 15, pp. 610–613, Aug. 2015, doi: 10.1109/LAWP.2015.2463108.
[21] S. Pandi, C. A. Balanis, and C. R. Birtcher, "Design of scalar impedance holographic metasurfaces for antenna beam formation with desired polarization," *IEEE Trans. Antennas Propag.*, vol. 63, no. 7, pp. 3016–3024, Jul. 2015, doi: 10.1109/TAP.2015.2426832.
[22] D. Sievenpiper, J. Schaffner, J. J. Lee, and S. Livingston, "A steerable leaky-wave antenna using a tunable impedance ground plane," *IEEE Antennas Wireless Propag. Lett.*, vol. 1, no. 1, pp. 179–182, 2002, doi: 10.1109/LAWP.2002.807788.
[23] D. F. Sievenpiper, J. H. Schaffner, H. J. Song, R. Y. Loo, and G. Tangonan, "Two-dimensional beam steering using an electrically tunable impedance surface," *IEEE Trans. Antennas Propag.*, vol. 51, no. 10, pp. 2713–2722, Oct. 2003, doi: 10.1109/TAP.2003.817558.
[24] D. F. Sievenpiper, "Forward and backward leaky wave radiation with large effective aperture from an electronically tunable textured surface," *IEEE Trans. Antennas Propag.*, vol. 53, no. 1, pp. 236–247, Jan. 2005, doi: 10.1109/TAP.2004.840516.
[25] J. L. Gómez-Tornero, F. D. Quesada-Pereira, and A. Álvarez-Melcón, "Analysis and design of periodic leaky-wave antennas for the millimeter waveband in hybrid waveguide-planar technology," *IEEE Trans. Antennas Propag.*, vol. 53, no. 9, pp. 2834–2842, Sep. 2005, doi: 10.1109/TAP.2005.854562.
[26] M. Li, S. Q. Xiao, and D. F. Sievenpiper, "Polarization-insensitive holographic surfaces with broadside radiation," *IEEE Trans. Antennas Propag.*, vol. 64, no. 12, pp. 5272–5280, Dec. 2016, doi: 10.1109/TAP.2016.2618853.
[27] M. G. Silveirinha, C. A. Fernandes, and J. R. Costa, "Electromagnetic characterization of textured surfaces formed by metallic pins," *IEEE Trans. Antennas Propag.*, vol. 56, no. 2, pp. 405–415, Feb. 2008, doi: 10.1109/TAP.2007.915442.
[28] G. Chattopadhyay, C. D. Jung-Kubiak, T. J. Reck, D. Gonzalez-Ovejero, and M. Alonso del Pino, "Low-profile and high-gain modulated metasurface antennas from gigahertz range frequencies," U.S. Patent Appl. No. 15/473,485, 2017.
[29] D. González-Ovejero, T. J. Reck, C. D. Jung-Kubiak, M. Alonso-Del-Pino, and G. Chattopadhyay, "A class of silicon micromachined metasurface for the design of high-gain terahertz antennas," in *Proc. IEEE Int. Symp. Antennas Propag. (APSURSI)*, Jun. 2016, pp. 1191–1192, doi: 10.1109/APS.2016.7696303.
[30] G. Minatti, F. Caminita, E. Martini, and S. Maci, "Flat optics for leaky-waves on modulated metasurfaces: Adiabatic Floquet-wave analysis," *IEEE Trans. Antennas Propag.*, vol. 64, no. 9, pp. 3896–3906, Sep. 2016, doi: 10.1109/TAP.2016.2590559.
[31] G. Minatti, F. Caminita, E. Martini, M. Sabbadini, and S. Maci, "Synthesis of modulated-metasurface antennas with amplitude, phase, and polarization control," *IEEE Trans. Antennas Propag.*, vol. 64, no. 9, pp. 3907–3919, Sep. 2016, doi: 10.1109/TAP.2016.2589969.
[32] G. Minatti, M. Faenzi, M. Sabbadini, and S. Maci, "Bandwidth of gain in metasurface antennas," *IEEE Trans. Antennas Propag.*, vol. 65, no. 6, pp. 2836–2842, Jun. 2017, doi: 10.1109/TAP.2017.2694769.
[33] G. Minatti, E. Martini, and S. Maci, "Efficiency of metasurface antennas," *IEEE Trans. Antennas Propag.*, vol. 65, no. 4, pp. 1532–1541, Apr. 2017, doi: 10.1109/TAP.2017.2669728.
[34] M. Faenzi *et al.*, "Metasurface antennas: New models, applications and realizations," *Sci. Rep.*, vol. 9, no. 1, p. 10,178, 2019, doi: 10.1038/s41598-019-46522-z.
[35] A. Tellechea Pereda *et al.*, "Dual circularly polarized broadside beam metasurface antenna," *IEEE Trans. Antennas Propag.*, vol. 64, no. 7, pp. 2944–2953, Jul. 2016, doi: 10.1109/TAP.2016.2562662.
[36] A. Tellechea Pereda *et al.*, "Experimental validation of a Ku-band dual-circularly polarized metasurface antenna," *IEEE Trans. Antennas Propag.*, vol. 66, no. 3, pp. 1153–1159, Mar. 2018, doi: 10.1109/TAP.2018.2794395.
[37] M. Faenzi, D. González-Ovejero, and S. Maci, "Wideband active region metasurface antennas," *IEEE Trans. Antennas Propag.*, vol. 68, no. 3, pp. 1261–1272, Mar. 2019, doi: 10.1109/TAP.2019.2940365.
[38] M. Faenzi, D. González-Ovejero, and S. Maci, "Flat gain broadband metasurface antennas," *IEEE Trans. Antennas Propag.*, vol. 69, no. 4, pp. 1942–1951, Apr. 2021, doi: 10.1109/TAP.2020.3026476.
[39] M. Faenzi, D. González-Ovejero, and S. Maci, "Overlapped and sequential metasurface modulations for Bi-Chromatic beams generation," *Appl. Phys. Lett.*, vol. 118, no. 18, p. 181,902, 2021, doi: 10.1063/5.0048985.
[40] M. Bodehou, C. Craeye, and I. Huynen, "Multifrequency band synthesis of modulated metasurface antennas," *IEEE Antennas Wireless Propag. Lett.*, vol. 19, no. 1, pp. 134–138, Jan. 2019, doi: 10.1109/LAWP.2019.2955895.
[41] D. González-Ovejero, G. Minatti, G. Chattopadhyay, and S. Maci, "Multibeam by metasurface antennas," *IEEE Trans. Antennas Propag.*, vol. 65, no. 6, pp. 2923–2930, Jun. 2017, doi: 10.1109/TAP.2017.2670622.
[42] M. Bodehou, E. Martini, S. Maci, I. Huynen, and C. Craeye, "Multibeam and beam scanning with modulated metasurfaces," *IEEE Trans. Antennas Propag.*, vol. 68, no. 3, pp. 1273–1281, Mar. 2020, doi: 10.1109/TAP.2019.2944554.
[43] N. Bodehou, "Modulated metasurface antennas: Analysis and direct numerical synthesis," Ph.D. dissertation, Univ. Catholique de Louvain, Louvain-La-Neuve, Belgium, 2020.
[44] M. Bodehou, C. Craeye, E. Martini, and I. Huynen, "A quasi-direct method for the surface impedance design of modulated metasurface antennas," *IEEE Trans. Antennas Propag.*, vol. 67, no. 1, pp. 24–36, Jan. 2019, doi: 10.1109/TAP.2018.2874762.
[45] M. Mencagli, E. Martini, and S. Maci, "Transition function for closed-form representation of metasurface reactance," *IEEE Trans. Antennas Propag.*, vol. 64, no. 1, pp. 136–145, Jan. 2016, doi: 10.1109/TAP.2015.2500264.
[46] F. Caminita and S. Maci, "New wine in old barrels: The use of the Oliner's method in metasurface antenna design," in *Proc. 44th Eur. Microw. Conf.*, Oct. 2014, pp. 437–439, doi: 10.1109/EuMC.2014.6986464.
[47] N. Engheta and R. W. Ziolkowski, Eds. *Metamaterials: Physics and Engineering Explorations*. Hoboken, NJ, USA: Wiley, 2006.
[48] S. Maci, M. Caiazzo, A. Cucini, and M. Casaletti, "A pole-zero matching method for EBG surfaces composed of a dipole FSS printed on a grounded dielectric slab," *IEEE Trans. Antennas Propag.*, vol. 53, no. 1, pp. 70–81, Jan. 2005, doi: 10.1109/TAP.2004.840520.
[49] A. Oliner and A. Hessel, "Guided waves on sinusoidally-modulated reactance surfaces," *IRE Trans. Antennas Propag.*, vol. 7, no. 5, pp. 201–208, 1959, doi: 10.1109/TAP.1959.1144771.
[50] S. Maci and A. Cucini, "FSS-based EBG surfaces," in Metamaterials, Physics and Engineering Explorations, N. Engheta and R. W. Ziolkowski, Eds. Hoboken, NJ, USA: Wiley, 2006, pp. 351–376.
[51] D. González-Ovejero and S. Maci, "Gaussian ring basis functions for the analysis of modulated metasurface antennas," *IEEE Trans. Antennas Propag.*, vol. 63, no. 9, pp. 3982–3993, Sep. 2015, doi: 10.1109/TAP.2015.2442585.
[52] M. Takahashi *et al.*, "Dual circularly polarized radial line slot antennas," *IEEE Trans. Antennas Propag.*, vol. 43, no. 8, pp. 874–876, Aug. 1995, doi: 10.1109/8.402208.

Open Access funding provided by 'University of Siena' within the CRUI CARE Agreement